iScience

CellPress
OPEN ACCESS

Article

Quantifying evolution of soot mixing state from transboundary transport of biomass burning emissions

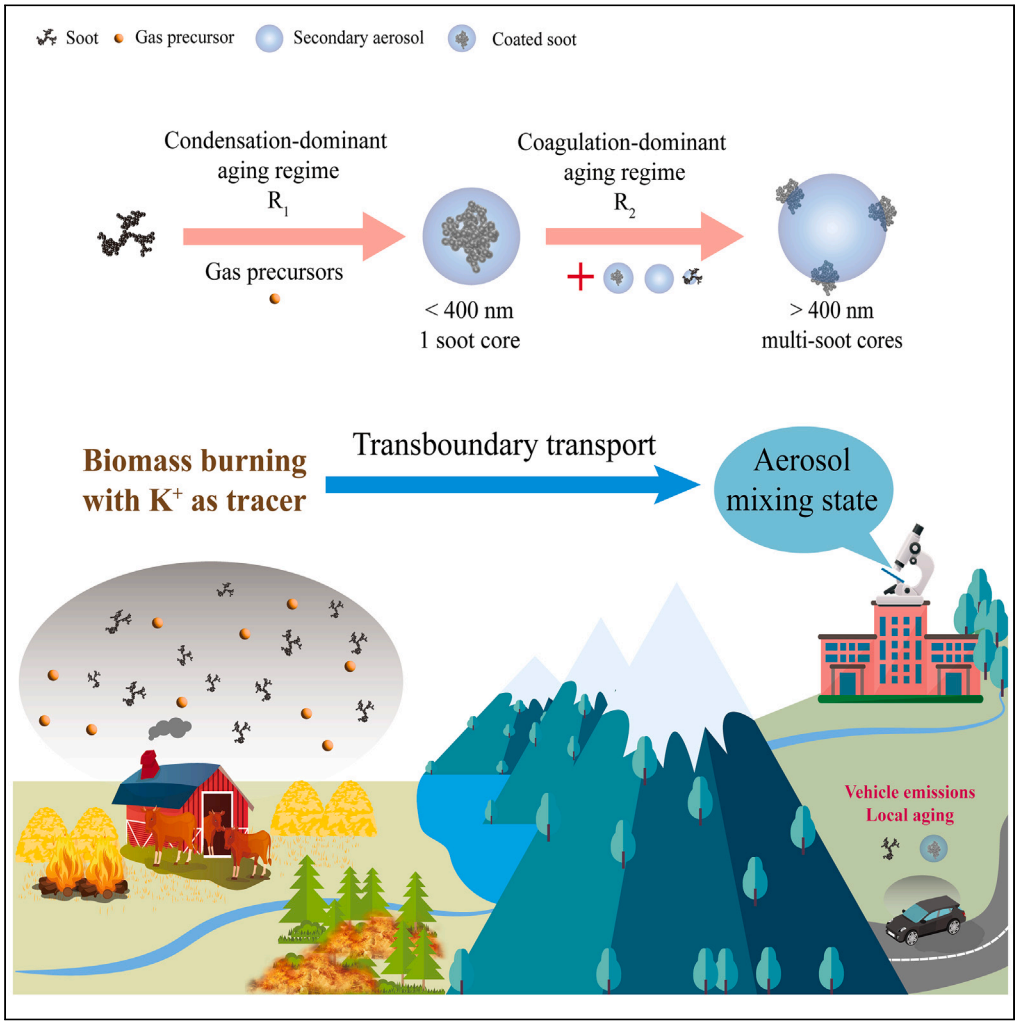

Xiyao Chen, Chunxiang Ye, Yuanyuan Wang, ..., Zongbo Shi, Zhonghua Zheng, Weijun Li

liweijun@zju.edu.cn

Highlights

Aged soot particles in southeastern Tibet came from biomass burning in South Asia

Condensation dominates fresh soot aging when particle diameter is <400 nm

Coagulation leads to multi-soot cores in a particle with diameter >400 nm

Stochastic nature of coagulation is confirmed in field studies for the first time

Chen et al., iScience *26*, 108125
November 17, 2023 © 2023 The Author(s).
https://doi.org/10.1016/j.isci.2023.108125

iScience

CellPress
OPEN ACCESS

Article

Quantifying evolution of soot mixing state from transboundary transport of biomass burning emissions

Xiyao Chen,[1] Chunxiang Ye,[2] Yuanyuan Wang,[1] Zhijun Wu,[2] Tong Zhu,[2] Fan Zhang,[1] Xiaokun Ding,[3] Zongbo Shi,[4] Zhonghua Zheng,[5] and Weijun Li[1,6,*]

SUMMARY

Incomplete combustion of fossil fuels and biomass burning emit large amounts of soot particles into the troposphere. The condensation process is considered to influence the size (D_p) and mixing state of soot particles, which affects their solar absorption efficiency and lifetimes. However, quantifying aging evolution of soot remains hampered in the real world because of complicated sources and observation technologies. In the Himalayas, we isolated soot sourced from transboundary transport of biomass burning and revealed soot aging mechanisms through microscopic observations. Most of coated soot particles stabilized one soot core under D_p < 400 nm, but 34.8% of them contained multi-soot cores ($n_{soot} \geq 2$) and n_{soot} increased 3–9 times with increasing D_p. We established the soot mixing models to quantify transformation from condensation- to coagulation-dominant regime at $D_p \approx 400$ nm. Studies provide essential references for adopting mixing rules and quantifying the optical absorption of soot in atmospheric models.

INTRODUCTION

Incomplete combustion of fossil fuels and biomass burning can emit large amounts of soot particles (i.e., black carbon) into the troposphere. Soot, a typical light-absorbing component of ambient aerosols, has a strong warming effect on climate with great uncertainties.[1–3] After emission, soot particles can mix with secondary aerosols through aging processes, i.e., condensation, coagulation, and cloud processes.[4] Aging processes can enhance the absorption of soot (E_{abs}) and make it efficient cloud condensation nuclei.[1] Because soot is nonvolatile and chemically inert, bulk measurements (such as total elemental carbon [EC] concentration) and global models often simplify the aging processes as the evolution of the particle-to-core diameter ratio (D_p/D_c), with assumptions that an individual particle only contains a single spherical soot core (n_{soot} = 1). That is, the diameter of this soot core (D_c) remains constant throughout the particle's lifetime.[4,5] However, previous studies have shown that these assumptions on the mixing state cause large uncertainties in the radiative effect and lifetime of soot-bearing particles.[6–11]

To constrain the uncertainties, some studies used more realistic morphology treatments and found that uncertainty due to the non-sphericity of soot-bearing particles occurred at low D_p/D_c (<1.4 or 1.7 in different studies).[7,12] These studies further emphasized the importance of characterizing and modeling the heterogeneity of D_p/D_c.[13,14] In addition, there is a negative relationship between D_p/D_c and D_c in some field studies.[15–18] The atmospheric condensation process has been considered the dominant regime to drive the above negative relationship: The fine soot core has a large relative surface area, and the same condensation mass could produce a larger D_p/D_c.[19,20] It seems a widely used theory to explain the heterogeneity of D_p/D_c, with the assumption that the contribution of coagulation to aging was negligible except very near the source.[4] However, current modeling studies proposed that the contribution of the coagulation mechanism was non-negligible and about 25% to the aging of soot in urban areas.[5] Mixing state modeling studies (e.g., Riemer et al.[21] and Matsui et al.[17]) further showed that the contribution of coagulation was about 4 times larger than the sum of other mechanisms, and the coagulation mechanism might lead to thickly coated soot particles (soot mass faction <20%). The heterogeneity of D_p/D_c is likely more attributed to the stochastic nature of the coagulation mechanism in the mixing state models (MSMs). Therefore, there is a knowledge gap on how aging processes control the heterogeneity in the per-particle D_p/D_c of soot-bearing particles between field studies and models. However, quantifying aging evolution of soot remains

[1]Key Laboratory of Geoscience Big Data and Deep Resource of Zhejiang Province, Department of Atmospheric Sciences, School of Earth Sciences, Zhejiang University, Hangzhou 310027, China
[2]College Environmental Sciences and Engineering, Peking University, Beijing 100871, China
[3]Department of Chemistry, Zhejiang University, Hangzhou 310027, China
[4]School of Geography, Earth and Environmental Sciences, University of Birmingham, Birmingham B15 2TT, UK
[5]Department of Earth and Environmental Sciences, The University of Manchester, Manchester M13 9PL, UK
[6]Lead contact
*Correspondence: liweijun@zju.edu.cn
https://doi.org/10.1016/j.isci.2023.108125

This is an open access article under the CC BY-NC-ND license (http://creativecommons.org/licenses/by-nc-nd/4.0/).

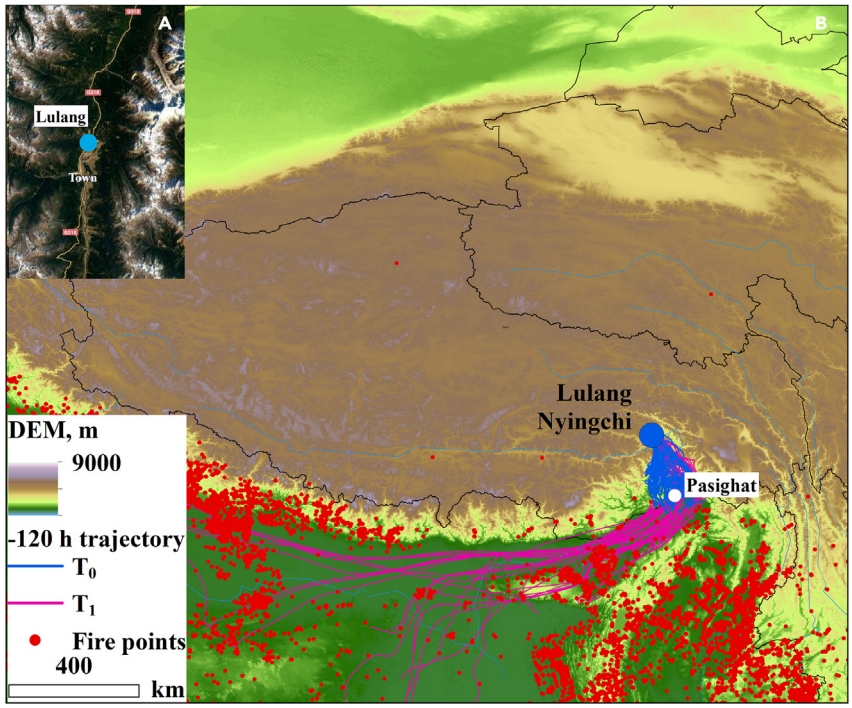

Figure 1. Location of Lulang station, Nyingchi, China and 120-h backward trajectories arriving at 500 m above ground level during the sampling periods

(A) A topographic map of the valley with the location of the sampling site.

(B) T_0 air masses came from high-altitude mountainous areas in the Himalayas. T_1 air masses transported farther and passed through intensive fire points in the Indo-Gangetic plain in South Asia. We ran the HYSPLIT model at the time of individual particle sampling.

hampered in the real world because of complicated emission sources and observation technologies.[11,22] Individual particle analysis has been confirmed as an effective method based on microscopic observations to capture the mixing state per particle and provides direct data to quantify aging evolution of soot.[23–25]

The Tibetan Plateau (TP), containing the most extensive glacial area outside of the Polar Regions, is known as the Asian Water Tower.[26] However, snow cover and glaciers are shrinking in the TP.[27] One of the main contributors is the increasing trend of soot emissions from fossil fuels and biomass burning (e.g., wildfires, mountain fires, and slash-and-burn agriculture fires), especially in South Asia.[28,29] The transboundary transported soot from biomass burning emissions in South Asia contributed to ~61.3% of surface soot mass in TP during the premonsoon season.[30] Previous studies showed that the valleys of the Himalayas, e.g., Lulang, were the great transport channel for vapor and soot from South Asia.[28,31] Therefore, the valleys of the Himalayas provide an ideal real-world laboratory to understand the aging mechanism of soot during transboundary transport. We quantified the distribution of D_p/D_c as a function of D_c and n_{soot} via microscopic observations for 3,113 soot-bearing particles. Our studies would provide essential references for quantifying evolution of soot mixing state from transboundary transport of biomass burning emissions.

RESULTS AND DISCUSSION

Chemical compositions of aerosol particles

At the Lulang sampling site (Figure 1), the mass concentrations of PM_{10} (particulate matter with aerodynamic diameter less than 10 μm) and EC were 16.5 ± 9.37 μg/m^3 and 0.28 ± 0.10 μg/m^3 during the sampling period, respectively. We found total water-soluble inorganic ions (TWSIIs) accounting for ~25% (Table S1), lower than the ~40% reported in urban and rural areas.[32] The ratio between organic carbon (OC) and EC (OC/EC) was 5.19 ± 2.34 which fell into the reported range of 4–14 in the TP (Table S2).

The strong correlation (>0.78) of EC with K^+ and SO_4^{2-} indicated that they mainly came from biomass burning through transboundary transport (Figure S1). Some field studies also proposed that about 80% of K^+ came from biomass burning in the Himalayas.[33,34] K^+/EC and NO_3^-/SO_4^{2-} are commonly used to identify the relative contributions of biomass burning and vehicle emissions in the atmosphere, respectively.[35,36] As a result, we identified two typical scenarios (Figure 2A): a low-K (LK) period in which NO_3^-/SO_4^{2-} peaks exceed 1 and K^+/EC is near zero; a high-K (HK) period in which NO_3^-/SO_4^{2-} decreases to 0.29 (gray line) and K^+/EC increases up to 0.44 (red line). These two scenarios are further confirmed by OC/EC values that are two times higher during the HK periods than during the LK periods (Table S3). A Hybrid Single-Particle Lagrangian Integrated Trajectory model (HYSPLIT)[37] was further used to compare the T_0 and T_1 air mass sources (Figure 1). T_0 air masses came from high-altitude mountainous areas in the Himalayas. T_1 air masses transported farther and passed through

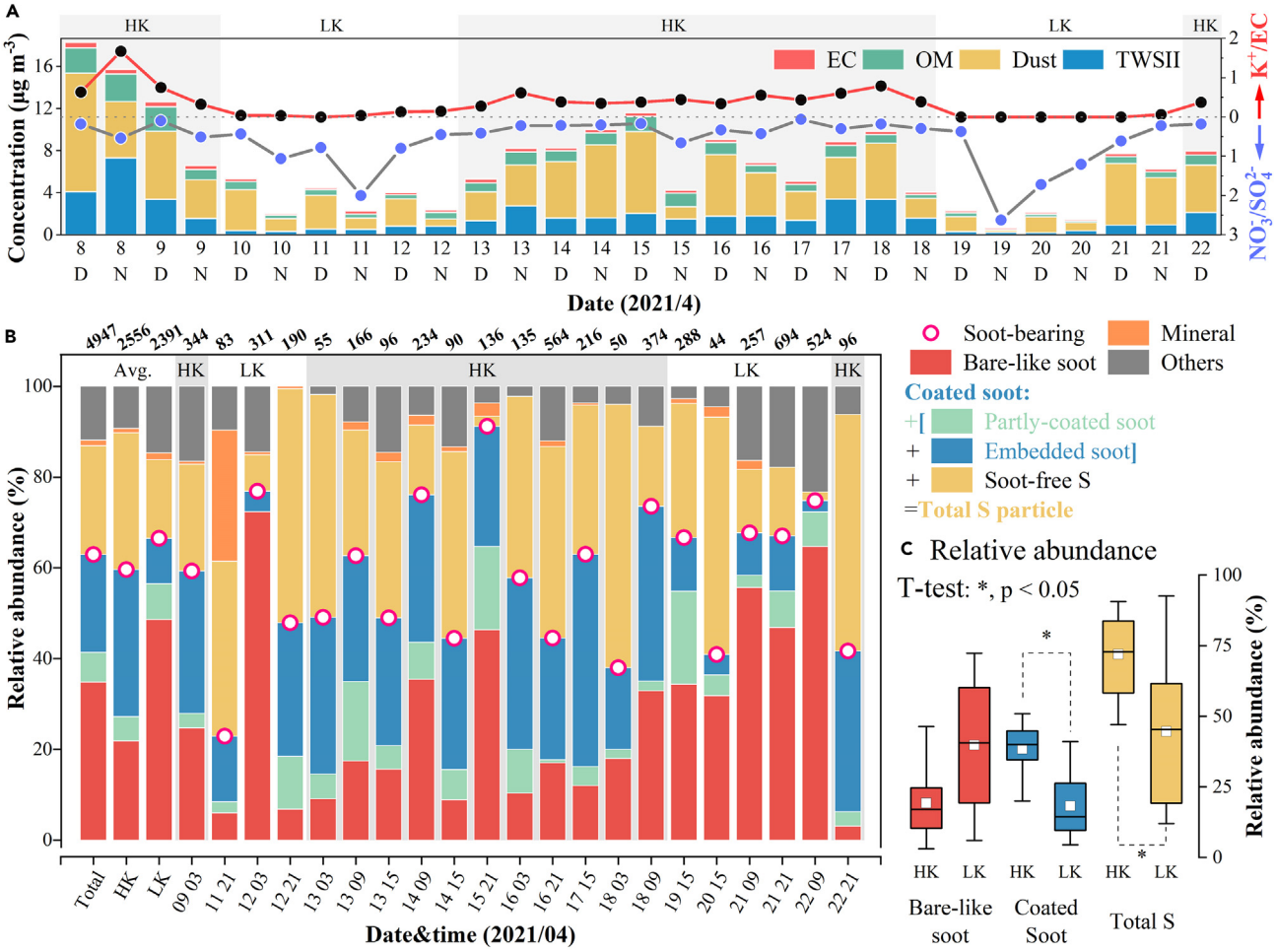

Figure 2. Variation of mass concentrations and different particle types

(A) Mass concentrations of the main components (D: daytime; N: nighttime), such as elemental carbon (EC), organic matter (OM), dust, and total water-soluble inorganic ions (TWSIIs). K^+/EC (red) and NO_3^-/SO_4^{2-} (gray) can indicate the relative contributions of biomass burning and vehicle emission, respectively.

(B) Variation of relative abundance of different particle types.

(C) The t test for the relative abundance of different types of particles. The boxplot shows the minimum, quartiles, maximum, respectively, and the white points are the mean value.

intensive fire points in the Indo-Gangetic plain in South Asia (Figure 1). Table S4 shows that 76% of trajectories were T_1 during HK periods, while 55% of trajectories were T_0 during LK periods. The Pasighat weather station is at the border of T_0 and T_1 (Figure 1). Pasighat was in dry and hot weather after rain, and Lulang was in the LK periods (Figure S2A). It suggested that wet deposition removed the transboundary-transported aerosol before the LK periods.[20] We also identified a haze layer over South Asia and a cloud layer in the Southeast TP from Moderate Resolution Imaging Spectroradiometer (MODIS) images during the HK periods (Figure S3). Based on our investigations, we preliminarily identified the LK and HK periods to be mainly influenced by vehicle emissions and biomass burning emissions, respectively. Therefore, the classification of HK and LK provides a unique opportunity to understand different soot aging mechanisms during transboundary transport in the real-world environment.

Characteristics of individual soot-bearing particles

Based on the morphology and mixing state of individual particles in transmission electron microscope (TEM) images, we classified the particles into four major types: soot-bearing, soot-free S-rich, mineral, and other particles (Text S1 and Figure S4). It is well known that individual soot particles with tens to hundreds of monomers displayed fractal-like aggregates and were mainly composed of elemental C (Figure S4l). Based on the relative position between soot and coating,[22] soot-bearing particles were classified into three subtypes: embedded, partly coated, and bare-like. An embedded soot particle indicates that the soot particle is completely enclosed in secondary S-rich aerosols (Figures 3a1–3a3). A partly coated soot particle means that one soot particle is partially attached or engulfed by secondary aerosols (Figures 3b1–3b3). A bare-like soot particle displays clear monomers and has almost no visible coating (Figures 3c1–3c3). The average

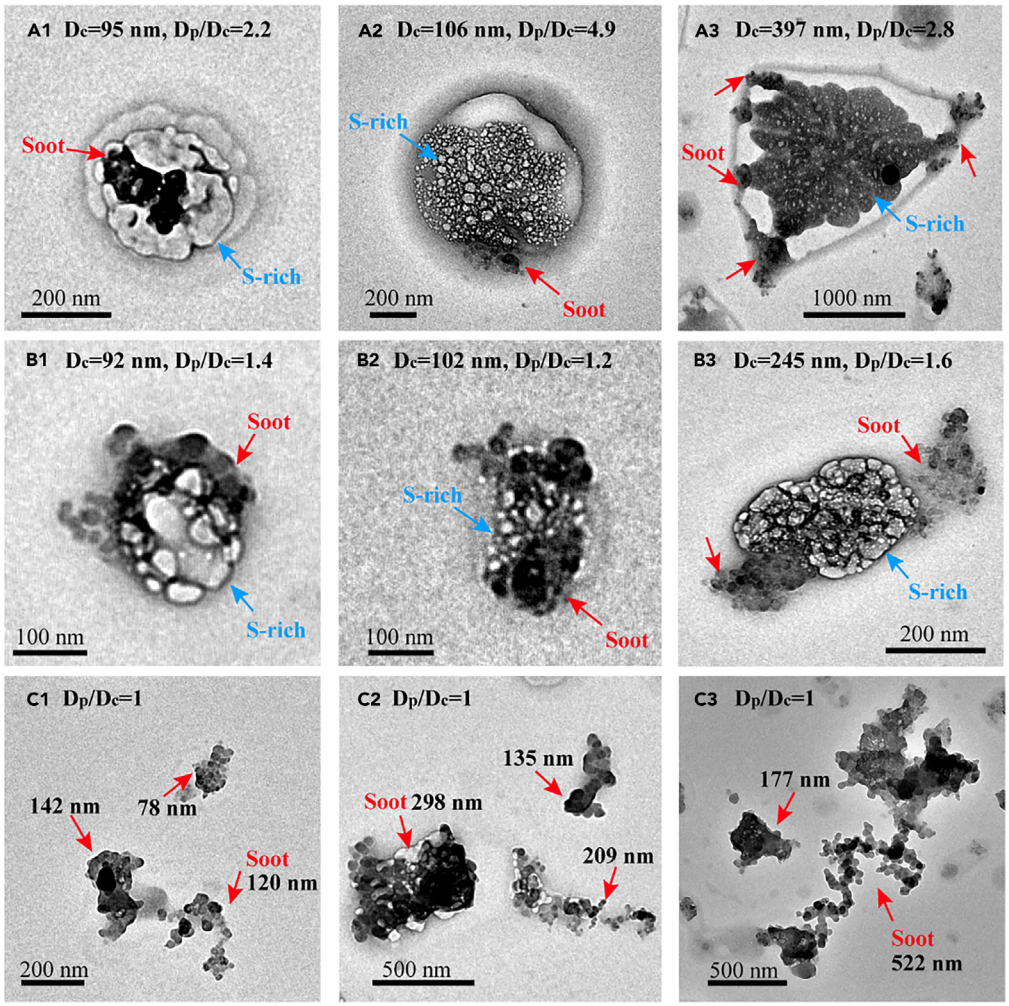

Figure 3. Transmission electron microscope (TEM) images of individual soot-bearing particles with different particle-to-core diameter ratio (D_p/D_c) and soot core size (D_c)

(A1–A3) Embedded soot particles.

(B1–B3) Partly coated soot particles.

(C1–C3) D_p/D_c is set as 1 for bare-like soot particles.

roundness (RN) of bare-like soot was 0.44, much lower than 0.52 for partly coated soot and 0.64 for embedded soot particles (Figure S5). In Figure S6, we further compared the fractal-like morphology of soot cores in soot-bearing particles via a fractal dimension (D_f). The D_f was 1.87 for bare-like soot, lower than 1.95 for partly coated soot and 2.06 for embedded soot. The highest D_f and RN of embedded soot represented the more compacted structure of the highly aged soot particles, and embedded soot particles were more spherical.[22,25,38]

Figure 2B shows that 63% of total analyzed particles were soot-bearing particles, which were slightly higher in LK periods (66%) than HK periods (59%). A t test was further applied to compare the relative abundance of different types of soot-bearing particles during the HK and LK periods (Table S5). We found that more soot remained bare-like during the LK periods. Compared to the LK periods, the relative number abundance increased ($p < 0.05$) by 27% for S-rich particles and by 20% for coated soot particles (i.e., the sum of embedded and partly coated soot particles) during the HK periods (Figure 2C). Figure S7 shows that number abundance of the embedded soot was 6 times higher than that of partly coated soot during the HK period, which is different from that of soot-bearing particles in urban air as the major type.[22,38] In summary, air masses through transboundary transport brought more S-rich particles and aged soot due to the biomass burning during the HK periods.

Size-resolved mixing state of soot

Figure 4 shows the distribution of D_p/D_c as a function of n_{soot} (Figure 4A) and D_c (Figure 4B). To understand the aging mechanism of individual soot particles through transboundary transport, we constructed Equation 1 as the soot MSM to represent the average trend for all coated soot between D_p/D_c and D_c:

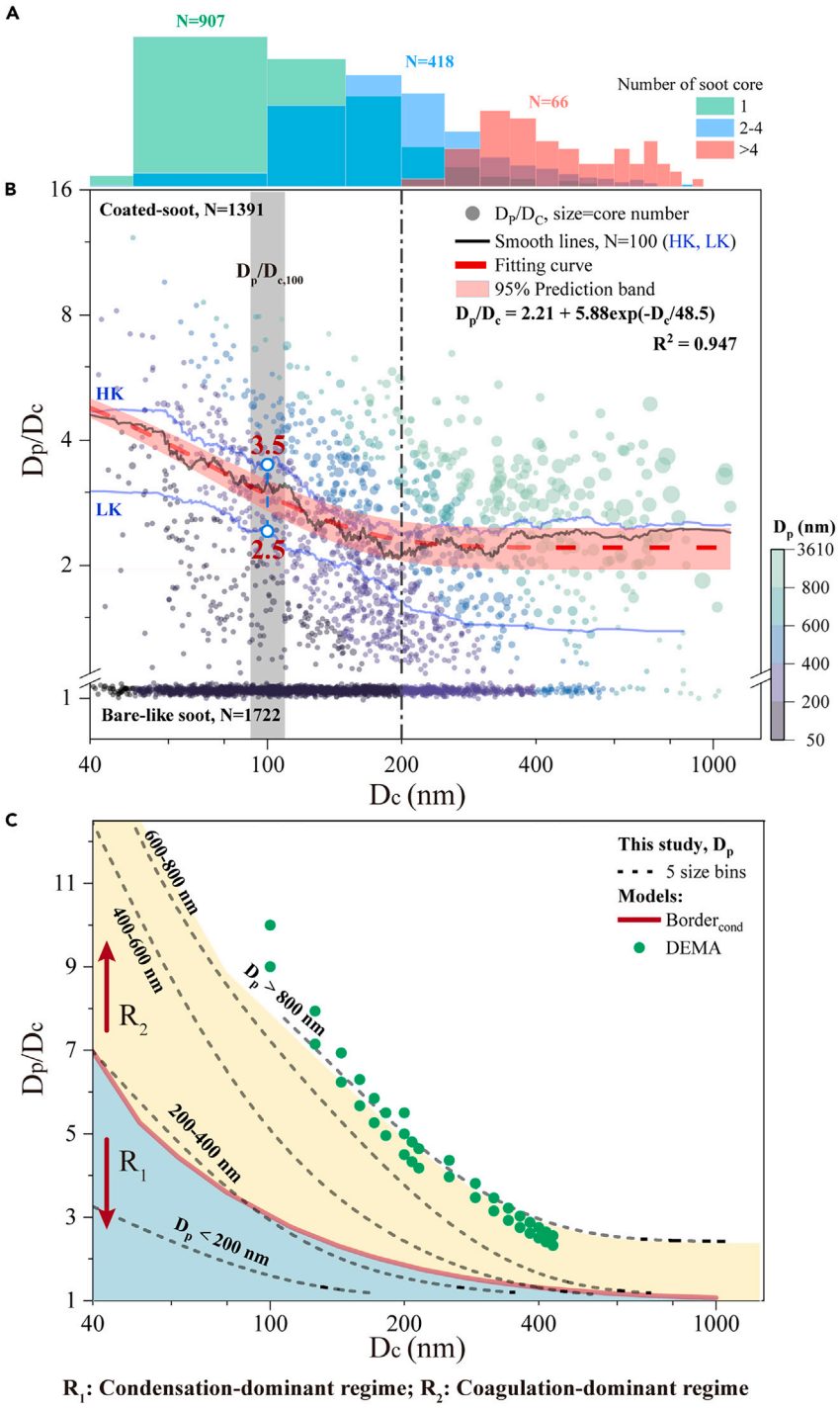

Figure 4. Two-dimension feature of particle-to-core diameter ratio (D_p/D_c) and soot core size (D_c). X axis is D_c in three figures

(A) Histogram is the frequency distribution of the soot core, and different colors represent the number of soot cores (n_{soot}) in each individual particle.

(B) Smooth lines (N = 100), are used for all coated soot particles (black), during the HK and LK periods (blue). Red line means the fitting curve for all coated soot particles.

(C) Dashed lines are fitting curves of the soot mixing state model (MSM) in Equation 3. The $border_{cond}$ means the max D_p/D_c versus D_c in the condensation model, described in Text S2. Green points represented the theoretical condition (Table S7) according to n_{soot} and the mixing rule of dynamic effective medium approximation (DEMA is detailed in "STAR Methods").

$$D_p / D_c = 2.21 + 5.88 \times Exp(-D_c / 48.5) \quad \text{(Equation 1)}$$

The above equation shows that D_p/D_c decreases with increasing D_c (Figure 4B: red dashed line). A similar declining trend under $D_c < 200$ nm was reported in previous studies using a single particle soot photometer (SP2).[16,20] D_p/D_c at $D_c = 100$ nm ($D_p/D_{c,100}$) was a useful tool to characterize the heterogeneity of D_p/D_c[4]. During the sampling period, the average $D_p/D_{c,100}$ at 3.5 in the HK periods was 40% higher than 2.5 during the LK periods (Figure 4B). Some studies also indicated that the range of $D_p/D_{c,100}$ became larger in transboundary transport events, e.g., during winter in Beijing (~2–5) and over the Indian Ocean (~3–7),[15,18] compared to the aging near the emission (~1–2).[18,39]

TEM images can more accurately display the morphology and mixing state of soot-bearing particles (Figure 3) and broader particle size (geometric standard deviation, $\sigma_g = 2.3$, Figure S8) compared to the SP2 ($\sigma_g = 1.4–1.9$).[11,19,22] Figure 4B shows that D_p/D_c reaches an equilibrium state of ~2.2 instead of continuously declining once $D_c > 200$ nm. We further assigned $D_c = 200$ nm as the boundary to understand the aging processes of soot particles. Interestingly, 34.8% of coated soot particles contained multi-soot cores ($n_{soot} \geq 2$) (Figure 4A) and were dominant (62.9%) when $D_c > 200$ nm (e.g., Figure 3a3). We noticed that the range of n_{soot} became larger as D_p increased (Figure S9), suggesting that there was a mechanism that increased n_{soot} during the aging processes. We further decoupled the MSM into two exponential decay processes ($ExpDec_i$, i = 1 and 2, in Equation 2) to identify the different aging mechanisms in different size bins.

$$D_p / D_c = [D_p/D_c]_e + A_1 \times Exp_1(-D_c / P_1) + A_2 \times Exp_2(-D_c / P_2) \quad \text{(Equation 2)}$$

where $[D_p/D_c]_e$ is the equilibrium state and indicates the average mixing state of large D_c in each size bin (e.g., Figures 3a3 and 3b2). $(-D_c/P_i)$ is the exponent of the $ExpDec_i$, showing the normalized driving power of D_c. Details are provided in Table S6. We obtained the specific MSM (Equation 3) for each size bin based on Equation 2.

$$D_p/D_c = \begin{cases} 1.1 + 5.7\ Exp_1(-D_c/42) & D_p \leq 200\ nm \\ 1.1 + 12\ Exp_1(-D_c/39) + 2.2\ Exp_2(-D_c/114) & 200 - 400\ nm \\ 1.1 + 22\ Exp_1(-D_c/32) + 7.2\ Exp_2(-D_c/118) & 400 - 600\ nm \\ 1.2 + 36\ Exp_1(-D_c/18) + 14\ Exp_2(-D_c/122) & 600 - 800\ nm \\ 2.4 + 12\ Exp_2(-D_c/128) & D_p \geq 800\ nm \end{cases} \quad \text{(Equation 3)}$$

The P_1 (18–42) is lower than P_2 (114–128) in MSM (Equation 3), suggesting that $ExpDec_1$ is more dependent on D_c than the $ExpDec_2$. Through the model evaluation statistics (Table S6), equations including $ExpDec_2$ significantly improve the predictability when particle size is >200 nm, and $ExpDec_2$ dominates the heterogeneity of D_p/D_c when D_p increased to 800 nm.

Based on the condensation model developed by Sedlacek et al.[4] (Text S2), Figure 4C displays a borderline (red line named $border_{cond}$) to represent the maximum D_p/D_c versus D_c under the condensation mechanism. We noticed that the fitting curve (dashed line in Figure 4C) for $D_p < 200$ nm was not beyond the $border_{cond}$ (red line). When D_p increased to 400 nm, the fitting curve strongly coincided with the $border_{cond}$ (Figure 4C). Therefore, we assigned $ExpDec_1$ to represent the condensation mechanism. Once $D_p > 400$ nm, Figure 4C shows that the fitting curves were beyond the $border_{cond}$, suggesting that the condensation mechanism did not dominate the increase in D_p/D_c. We found that the range of n_{soot} became larger as D_p increases: e.g., n_{soot} stabilizes at 1 under $D_p < 400$ nm, while n_{soot} varies 1–3 for D_p at 400–600 nm and 1–5 for D_p at 600–800 nm (Figure S9). According to the mixing rule of dynamic effective medium approximation (DEMA) shown in STAR Methods, the heterogeneity of D_p/D_c is determined more by the n_{soot} involved in the coagulation for a selected size bin.[8,40] Figure 4C shows that the DEMA could well explain the heterogeneity of D_p/D_c when $D_p \geq 800$ nm (green points in Figure 4C). Therefore, the $ExpDec_2$ as shown in Equation 3 was assigned to represent the coagulation mechanism.

We further applied our above findings to classify soot particles collected in Amakusa city of Japan, one downstream of East Asia.[38] More information is in Xu et al.[38] There were 40% of coated soot particles with $n_{soot} \geq 2$ during one transboundary transport event. Figure S10 shows that the range of n_{soot} stabilized at 1 under $D_p < 400$ nm and became larger with the increasing D_p. Moreover, Matsui et al.[17] developed a MSM to simulate a similar transport event from China to Japan and proposed that the condensation process was dominant for the growth of thinly coated soot particles, while the coagulation process was necessary to produce thickly coated soot particles during transboundary transport. Therefore, we can confirm that the stochastic nature of coagulation dominated the heterogeneity of the soot mixing state via increasing n_{soot} and D_c during transboundary transport.

According to the Brownian coagulation theory shown by Seinfeld and Pandis,[41] the coagulation is the balanced result between coagulation efficiency (K_{cog}) and the number concentration of particles, and K_{cog} between two dry particles theoretically increased ($2.5–5.5 \times 10^{-6}$ cm^3/h) with the difference in their sizes (D_{p1}, D_{p2}) (Figure S11 and Text S3). Some studies reported that the number concentration of sub-100 nm particles was about 200–400 cm^{-3} in the TP,[16,42] which fell into the typical number distribution of background particles in remote areas.[41] Riemer et al.[21] simulated the coagulation among soot particles and background particles (i.e., secondary particles) and found that the mass of thickly coated soot increased by 426% when coagulation was included within 24 h. Due to sufficient aging time, the continuous coagulation process could cause the individual particle to contain multi-soot cores in transboundary transport. Moreover, the hygroscopic secondary coating easily promotes soot particle activation into cloud condensation nuclei.[2] When considering hygroscopicity, average K_{cog} is 6×10^{-6} cm^3/h in Fierce et al.[43] and larger than K_{cog} for dry particles ($2.5–5.5 \times 10^{-6}$ cm^3/h in Text S3).

Therefore, we proposed two aging mechanisms and mixing rules for soot particles during transboundary transport: R_1, condensation-dominant regime, and R_2, coagulation-dominant regime (Figure 4C). For the R_1, an individual particle ($D_p < 400$ nm) contains one soot core (Figures S9 and S10). The well-known core-shell mixing rule could be used to simplify soot morphology and mixing structure.[24,44] Indeed,

some studies have developed robust and empirical methods to correct the overestimation of optical absorption under the core-shell mixing rule.[7,12,45] However, these improved core-shell models still could not precisely evaluate the optical absorption of various aged soot particles. Recently, Wang et al.[46] proposed an electron-microscope-to-BC-simulation (EMBS) model to consider the embedded fraction (i.e., the volume ratio of the soot core that is covered in the coating) and morphology of individual particles by a discrete dipole approximation. They proposed that the morphology and the embedded fraction of aged soot particles can significantly influence approximately 29% and 80% of the absorption enhancement of aged soot particles, respectively.[46] Therefore, attention needs to be given to the micro-physical changes (e.g., morphology, embedded fraction, and D_p/D_c) in soot particles at the R_1 stage.

For the R_2, an individual particle (D_p > 400 nm) normally bears two or more soot cores (Figures S9 and S10). The stochastic nature of coagulation could cause the aerosol particles with multi-soot cores due to sufficient aging time in transboundary transport. Figure 4C shows that the D_p/D_c values for the R_2 are much higher than those for R_1. The morphology and embedded fraction of soot particles are no longer considered to dominate optical absorption. Compared to the core-shell mixing rule, Jacobson[40] proposed that the particles with multi-soot cores could absorb more visible light by a DEMA method. Interestingly, we found that soot cores commonly distributed in the organic coating in TEM images (e.g., Figures 3a2–3a3) were not random as described in DEMA. Zhang et al.[23] proposed that some soot embedded within individual particles can be redistributed from the central inorganic phase to the organic coating phase under liquid-liquid phase separation (LLPS) in the atmosphere. The soot redistribution could reduce the absorption enhancement effect by 28%–34% compared to the core-shell model.[23] Therefore, more attention should be given to the soot redistribution influenced by the LLPS at the R_2 stage.

Limitations of the study

Field studies often assume that the condensation can dominate the heterogeneity of D_p/D_c.[4,20] The bulk model assumes that the number size distribution of D_c remains constant during aging, and the mean contribution of coagulation to the total aging of soot is estimated just less than 25%.[5] Aforementioned assumptions are not scientific enough and will cause an underestimation of the importance of coagulation between soot and accumulation mode aerosol. Therefore, Riemer et al.[21] and Matsui et al.[8] treated detailed coagulation processes in the MSMs and proposed that the possible coagulation mechanisms might lead to thickly coated soot particles and multi-soot cores in accumulation mode particles. We found that the number of soot cores in an individual particle (n_{soot}) increased 3–9 times with the increasing D_p, rather than stabilizing at 1 in the real-world air. Interestingly, 62.9% of coated soot particles with D_c > 200 nm contained multi-soot cores ($n_{soot} \geq 2$).

For the first time, we confirmed that the stochastic nature of coagulation dominated the heterogeneity of the mixing state of soot via increasing n_{soot} and D_c during transboundary transport. We established the soot MSMs to quantify transformation from condensation- to coagulation-dominant regime at $D_p \approx 400$ nm, when the condensation mechanism is at equilibrium at about D_p = 400 nm. Our MSM could be applied to further parametrize the evolution of the soot mixing state and save computational costs for Riemer et al.[21] and Matsui et al.,[8] which are computationally too expensive to apply to 3D calculations. Moreover, our studies provide important references for studies to select detailed mixing rules for optical calculations in two aspects: First, more work is needed to correct the core-shell model based on the morphology of soot and coating in the condensation-dominant regime. Second, we confirm for the first time that the DEMA can be applied to replace the core-shell mixing rules in the coagulation-dominant regime due to multi-soot cores. DEMA is more accurate and sophisticated than core-shell model, and it has developed for over forty years to calculate optical parameters of particles with multi-soot cores.[8,40,47] We provide the observational evidence to understand how a soot ages into a particle with multi-soot cores during their atmospheric transports.[48] We also propose that the position of soot cores and liquid-liquid phase separation are critical factors in the coagulation-dominant regime to further optimize DEMA in the future. These two regimes developed in the field campaign better cover the soot mixing rules adopted in the current atmospheric models and further precisely quantify the optical absorption of aged soot particles in the atmosphere.

STAR★METHODS

Detailed methods are provided in the online version of this paper and include the following:

- KEY RESOURCES TABLE
- RESOURCE AVAILABILITY
  - Lead contact
  - Materials availability
  - Data and code availability
- METHOD DETAILS
  - Aerosol collection and measurement
  - Individual particle collection and morphological analysis
  - Mixing rules for soot-bearing particles in the models

SUPPLEMENTAL INFORMATION

Supplemental information can be found online at https://doi.org/10.1016/j.isci.2023.108125.

ACKNOWLEDGMENTS

This work was funded by the National Natural Science Foundation of China (42075096; 42277080), Zhejiang Provincial Basic Commonweal Project (Grant No. LGC22B050009), and Fundamental Research Funds for the Central Universities (No. K20220232). The authors acknowledge staff of the South-East Tibetan Plateau Station for Integrated Observation and Research of Alpine Environment in Lulang for sample collecting.

AUTHOR CONTRIBUTIONS

X.C. and W.L. conceived the overall idea and performed most of the analysis and model simulations; X.C., F.Z., and Y.W. drafted the paper; T.Z., W.Z., Z.S., and Z.Z. edited the paper; C.Y. collected the samples; X.D. conducted the experiment.

DECLARATION OF INTERESTS

The authors declare no competing interests.

Received: June 21, 2023
Revised: September 14, 2023
Accepted: September 28, 2023
Published: October 4, 2023

REFERENCES

1. Bond, T.C., Doherty, S.J., Fahey, D.W., Forster, P.M., Berntsen, T., DeAngelo, B.J., Flanner, M.G., Ghan, S., Kärcher, B., Koch, D., et al. (2013). Bounding the role of black carbon in the climate system: A scientific assessment. J. Geophys. Res. Atmos. *118*, 5380–5552. https://doi.org/10.1002/jgrd.50171.
2. Coppola, A.I., Wagner, S., Lennartz, S.T., Seidel, M., Ward, N.D., Dittmar, T., Santín, C., and Jones, M.W. (2022). The black carbon cycle and its role in the Earth system. Nat. Rev. Earth Environ. *3*, 516–532. https://doi.org/10.1038/s43017-022-00316-6.
3. Ranasinghe, R., Ruane, A.C., Vautard, R., Arnell, N., Coppola, E., Cruz, F.A., Dessai, S., Islam, A.S., Rahimi, M., Carrascal, D.R., et al. (2021). Climate Change Information for Regional Impact and for Risk Assessment. In Climate Change 2021: The Physical Science Basis. Contribution of Working Group I to the Sixth Assessment Report of the Intergovernmental Panel on Climate Change (Cambridge University Press).
4. Sedlacek, A.J., 3rd, Lewis, E.R., Onasch, T.B., Zuidema, P., Redemann, J., Jaffe, D., and Kleinman, L.I. (2022). Using the black carbon particle mixing state to characterize the lifecycle of biomass burning aerosols. Environ. Sci. Technol. *56*, 14315–14325. https://doi.org/10.1021/acs.est.2c03851.
5. Shen, W., Wang, M., Liu, Y., Dong, X., Zhao, D., Yue, M., Tian, P., and Ding, D. (2023). Evaluating BC Aging Processes in the Community Atmosphere Model Version 6 (CAM6). JGR. Atmospheres *128*. https://doi.org/10.1029/2022jd037427.
6. Brown, H., Liu, X., Pokhrel, R., Murphy, S., Lu, Z., Saleh, R., Mielonen, T., Kokkola, H., Bergman, T., Myhre, G., et al. (2021). Biomass burning aerosols in most climate models are too absorbing. Nat. Commun. *12*, 277. https://doi.org/10.1038/s41467-020-20482-9.
7. Liu, D., Whitehead, J., Alfarra, M., Reyes-Villegas, E., Spracklen, D., Reddington, C., Kong, S., Williams, P., Ting, Y.-C., Haslett, S., et al. (2017). Black-carbon absorption enhancement in the atmosphere determined by particle mixing state. Nat. Geosci. *10*, 184–188. https://doi.org/10.1038/ngeo2901.
8. Matsui, H., Hamilton, D.S., and Mahowald, N.M. (2018). Black carbon radiative effects highly sensitive to emitted particle size when resolving mixing-state diversity. Nat. Commun. *9*, 3446. https://doi.org/10.1038/s41467-018-05635-1.
9. Zheng, Z., West, M., Zhao, L., Ma, P.-L., Liu, X., and Riemer, N. (2021). Quantifying the structural uncertainty of the aerosol mixing state representation in a modal model. Atmos. Chem. Phys. *21*, 17727–17741. https://doi.org/10.5194/acp-21-17727-2021.
10. Yao, Y., Curtis, J.H., Ching, J., Zheng, Z., and Riemer, N. (2022). Quantifying the effects of mixing state on aerosol optical properties. Atmos. Chem. Phys. *22*, 9265–9282. https://doi.org/10.5194/acp-22-9265-2022.
11. Zhang, Y., Su, H., Kecorius, S., Ma, N., Wang, Z., Sun, Y., Zhang, Q., Pöschl, U., Wiedensohler, A., Andreae, M.O., and Cheng, Y. (2023). Extremely low-volatility organic coating leads to underestimation of black carbon climate impact. One Earth *6*, 158–166. https://doi.org/10.1016/j.oneear.2023.01.009.
12. Fierce, L., Onasch, T.B., Cappa, C.D., Mazzoleni, C., China, S., Bhandari, J., Davidovits, P., Fischer, D.A., Helgestad, T., Lambe, A.T., et al. (2020). Radiative absorption enhancements by black carbon controlled by particle-to-particle heterogeneity in composition. Proc. Natl. Acad. Sci. USA *117*, 5196–5203. https://doi.org/10.1073/pnas.1919723117.
13. Fierce, L., Bond, T.C., Bauer, S.E., Mena, F., and Riemer, N. (2016). Black carbon absorption at the global scale is affected by particle-scale diversity in composition. Nat. Commun. *7*, 12361. https://doi.org/10.1038/ncomms12361.
14. Zhai, J., Yang, X., Li, L., Bai, B., Liu, P., Huang, Y., Fu, T.M., Zhu, L., Zeng, Z., Tao, S., et al. (2022). Absorption enhancement of black carbon aerosols constrained by mixing-state heterogeneity. Environ. Sci. Technol. *56*, 1586–1593. https://doi.org/10.1021/acs.est.1c06180.
15. Kompalli, S.K., Babu, S.N.S., Moorthy, K.K., Satheesh, S.K., Gogoi, M.M., Nair, V.S., Jayachandran, V.N., Liu, D., Flynn, M.J., and Coe, H. (2021). Mixing state of refractory black carbon aerosol in the South Asian outflow over the northern Indian Ocean during winter. Atmos. Chem. Phys. *21*, 9173–9199. https://doi.org/10.5194/acp-21-9173-2021.
16. Tan, T., Hu, M., Du, Z., Zhao, G., Shang, D., Zheng, J., Qin, Y., Li, M., Wu, Y., Zeng, L., et al. (2021). Measurement report: Strong light absorption induced by aged biomass burning black carbon over the southeastern Tibetan Plateau in pre-monsoon season. Atmos. Chem. Phys. *21*, 8499–8510. https://doi.org/10.5194/acp-21-8499-2021.
17. Matsui, H., Koike, M., Kondo, Y., Moteki, N., Fast, J.D., and Zaveri, R.A. (2013). Development and validation of a black carbon mixing state resolved three-dimensional model: Aging processes and radiative impact. J. Geophys. Res. Atmos. *118*, 2304–2326. https://doi.org/10.1029/2012jd018446.
18. Liu, D., Joshi, R., Wang, J., Yu, C., Allan, J.D., Coe, H., Flynn, M.J., Xie, C., Lee, J., Squires, F., et al. (2019). Contrasting physical properties of black carbon in urban Beijing between winter and summer. Atmos. Chem. Phys. *19*, 6749–6769. https://doi.org/10.5194/acp-19-6749-2019.
19. Zhao, G., Tan, T., Hu, S., Du, Z., Shang, D., Wu, Z., Guo, S., Zheng, J., Zhu, W., Li, M., et al. (2022). Mixing state of black carbon at different atmospheres in north and southwest China. Atmos. Chem. Phys. *22*, 10861–10873. https://doi.org/10.5194/acp-22-10861-2022.
20. Wang, Q., Cao, J., Han, Y., Tian, J., Zhu, C., Zhang, Y., Zhang, N., Shen, Z., Ni, H., Zhao, S., and Wu, J. (2018). Sources and physicochemical characteristics of black carbon aerosol from the southeastern Tibetan Plateau: internal mixing enhances light absorption. Atmos. Chem. Phys. *18*, 4639–4656. https://doi.org/10.5194/acp-18-4639-2018.
21. Riemer, N., West, M., Zaveri, R.A., and Easter, R.C. (2009). Simulating the evolution of soot mixing state with a particle-resolved aerosol model. J. Geophys. Res. *114*, D09202. https://doi.org/10.1029/2008jd011073.

22. Wang, Y., Liu, F., He, C., Bi, L., Cheng, T., Wang, Z., Zhang, H., Zhang, X., Shi, Z., and Li, W. (2017). Fractal dimensions and mixing structures of soot particles during atmospheric processing. Environ. Sci. Technol. Lett. *4*, 487–493. https://doi.org/10.1021/acs.estlett.7b00418.
23. Zhang, J., Wang, Y., Teng, X., Liu, L., Xu, Y., Ren, L., Shi, Z., Zhang, Y., Jiang, J., Liu, D., et al. (2022). Liquid-liquid phase separation reduces radiative absorption by aged black carbon aerosols. Commun. Earth Environ. *3*, 128. https://doi.org/10.1038/s43247-022-00462-1.
24. Adachi, K., Chung, S.H., and Buseck, P.R. (2010). Shapes of soot aerosol particles and implications for their effects on climate. J. Geophys. Res. *115*, D15206. https://doi.org/10.1029/2009jd012868.
25. China, S., Mazzoleni, C., Gorkowski, K., Aiken, A.C., and Dubey, M.K. (2013). Morphology and mixing state of individual freshly emitted wildfire carbonaceous particles. Nat. Commun. *4*, 2122. https://doi.org/10.1038/ncomms3122.
26. Yao, T., Bolch, T., Chen, D., Gao, J., Immerzeel, W., Piao, S., Su, F., Thompson, L., Wada, Y., Wang, L., et al. (2022). The imbalance of the Asian water tower. Nat. Rev. Earth Environ. *3*, 618–632. https://doi.org/10.1038/s43017-022-00299-4.
27. Maurer, J.M., Schaefer, J.M., Rupper, S., and Corley, A. (2019). Acceleration of ice loss across the Himalayas over the past 40 years. Sci. Adv. *5*, eaav7266. https://doi.org/10.1126/sciadv.aav7266.
28. Li, C., Yan, F., Kang, S., Yan, C., Hu, Z., Chen, P., Gao, S., Zhang, C., He, C., Kaspari, S., and Stubbins, A. (2021). Carbonaceous matter in the atmosphere and glaciers of the Himalayas and the Tibetan plateau: An investigative review. Environ. Int. *146*, 106281. https://doi.org/10.1016/j.envint.2020.106281.
29. Xue, T., Geng, G., Han, Y., Wang, H., Li, J., Li, H.T., Zhou, Y., and Zhu, T. (2021). Open fire exposure increases the risk of pregnancy loss in South Asia. Nat. Commun. *12*, 3205. https://doi.org/10.1038/s41467-021-23529-7.
30. Yang, J., Kang, S., Ji, Z., and Chen, D. (2018). Modeling the Origin of Anthropogenic Black Carbon and Its Climatic Effect Over the Tibetan Plateau and Surrounding Regions. JGR. Atmospheres *123*, 671–692. https://doi.org/10.1002/2017jd027282.
31. Wu, G., Wan, X., Ram, K., Li, P., Liu, B., Yin, Y., Fu, P., Loewen, M., Gao, S., Kang, S., et al. (2020). Light absorption, fluorescence properties and sources of brown carbon aerosols in the Southeast Tibetan Plateau. Environ. Pollut. *257*, 113616. https://doi.org/10.1016/j.envpol.2019.113616.
32. Daellenbach, K.R., Uzu, G., Jiang, J., Cassagnes, L.E., Leni, Z., Vlachou, A., Stefenelli, G., Canonaco, F., Weber, S., Segers, A., et al. (2020). Sources of particulate-matter air pollution and its oxidative potential in Europe. Nature *587*, 414–419. https://doi.org/10.1038/s41586-020-2902-8.
33. Cong, Z., Kang, S., Kawamura, K., Liu, B., Wan, X., Wang, Z., Gao, S., and Fu, P. (2015). Carbonaceous aerosols on the south edge of the Tibetan Plateau: concentrations, seasonality and sources. Atmos. Chem. Phys. *15*, 1573–1584. https://doi.org/10.5194/acp-15-1573-2015.
34. Arun, B.S., Gogoi, M.M., Hegde, P., Borgohain, A., Boreddy, S.K.R., Kundu, S.S., and Babu, S.S. (2021). Carbonaceous Aerosols over Lachung in the Eastern Himalayas: Primary Sources and Secondary Formation of Organic Aerosols in a Remote High-Altitude Environment. ACS Earth Space Chem. *5*, 2493–2506. https://doi.org/10.1021/acsearthspacechem.1c00190.
35. Li, H., Zhang, Q., Duan, F., Zheng, B., and He, K. (2016). The "Parade Blue": effects of short-term emission control on aerosol chemistry. Faraday Discuss *189*, 317–335. https://doi.org/10.1039/c6fd00004e.
36. Zhang, J., Liu, L., Xu, L., Lin, Q., Zhao, H., Wang, Z., Guo, S., Hu, M., Liu, D., Shi, Z., et al. (2020). Exploring wintertime regional haze in northeast China: role of coal and biomass burning. Atmos. Chem. Phys. *20*, 5355–5372. https://doi.org/10.5194/acp-20-5355-2020.
37. Stein, A.F., Draxler, R.R., Rolph, G.D., Stunder, B.J.B., Cohen, M.D., and Ngan, F. (2015). NOAA's HYSPLIT Atmospheric Transport and Dispersion Modeling System. Bull. Am. Meteorol. Soc. *96*, 2059–2077. https://doi.org/10.1175/bams-d-14-00110.1.
38. Xu, L., Fukushima, S., Sobanska, S., Murata, K., Naganuma, A., Liu, L., Wang, Y., Niu, H., Shi, Z., Kojima, T., et al. (2020). Tracing the evolution of morphology and mixing state of soot particles along with the movement of an Asian dust storm. Atmos. Chem. Phys. *20*, 14321–14332. https://doi.org/10.5194/acp-20-14321-2020.
39. Hu, K., Liu, D., Tian, P., Wu, Y., Deng, Z., Wu, Y., Zhao, D., Li, R., Sheng, J., Huang, M., et al. (2021). Measurements of the diversity of shape and mixing state for ambient black carbon particles. Geophys. Res. Lett. *48*, e2021GL094522. https://doi.org/10.1029/2021gl094522.
40. Jacobson, M.Z. (2006). Effects of externally-through-internally-mixed soot inclusions within clouds and precipitation on global climate. J. Phys. Chem. A *110*, 6860–6873. https://doi.org/10.1021/jp056391r.
41. Seinfeld, J.H., and Pandis, S.N. (2016). Atmospheric Chemistry and Physics from Air Pollution to Climate Change (John Wiley & Sons, Inc.).
42. Bianchi, F., Junninen, H., Bigi, A., Sinclair, V.A., Dada, L., Hoyle, C.R., Zha, Q., Yao, L., Ahonen, L.R., Bonasoni, P., et al. (2020). Biogenic particles formed in the Himalaya as an important source of free tropospheric aerosols. Nat. Geosci. *14*, 4–9. https://doi.org/10.1038/s41561-020-00661-5.
43. Riemer, N., Bond, T.C., and Bond, T.C. (2017). Toward Reduced Representation of Mixing State for Simulating Aerosol Effects on Climate. Bull. Am. Meteorol. Soc. *98*, 971–980. https://doi.org/10.1175/bams-d-16-0028.1.
44. Kahnert, M., and Kanngießer, F. (2020). Modelling optical properties of atmospheric black carbon aerosols. J. Quant. Spectrosc. Radiat. Transf. *244*, 106849. https://doi.org/10.1016/j.jqsrt.2020.106849.
45. Zhai, J., Yang, X., Li, L., Ye, X., Chen, J., Fu, T.M., Zhu, L., Shen, H., Ye, J., Wang, C., and Tao, S. (2022). Direct observation of the transitional stage of mixing-state-related absorption enhancement for atmospheric black carbon. Geophys. Res. Lett. *49*, e2022GL101368. https://doi.org/10.1029/2022gl101368.
46. Wang, Y., Pang, Y., Huang, J., Bi, L., Che, H., Zhang, X., and Li, W. (2021). Constructing shapes and mixing structures of black carbon particles with applications to optical calculations. JGR. Atmospheres *126*, e2021JD034620. https://doi.org/10.1029/2021jd034620.
47. Chýlek, P., Ramaswamy, V., and Cheng, R.J. (1984). Effect of graphitic carbon on the albedo of clouds. J. Atmos. Sci. *41*, 3076–3084.
48. Wang, Z., Zhang, H., Li, J., Jing, X., and Lu, P. (2013). Radiative forcing and climate response due to the presence of black carbon in cloud droplets. J. Geophys. Res. Atmos. *118*, 3662–3675. https://doi.org/10.1002/jgrd.50312.
49. Zhao, Z., Cao, J., Shen, Z., Xu, B., Zhu, C., Chen, L.W.A., Su, X., Liu, S., Han, Y., Wang, G., and Ho, K. (2013). Aerosol particles at a high-altitude site on the Southeast Tibetan Plateau, China: Implications for pollution transport from South Asia. J. Geophys. Res. Atmos. *118*, 11360–11375. https://doi.org/10.1002/jgrd.50599.
50. Zhang, L., Tang, C., Huang, J., Du, T., Guan, X., Tian, P., Shi, J., Cao, X., Huang, Z., Guo, Q., et al. (2021). Unexpected high absorption of atmospheric aerosols over a western Tibetan Plateau site in summer. JGR. Atmospheres *126*, e2020JD033286. https://doi.org/10.1029/2020jd033286.
51. Brasil, A.M., Farias, T.L., and Carvalho, M.G. (1999). A Recipe for Image Characterization of Fractal-Like Aggregates. J. Aerosol Sci. *30*, 1379–1389.
52. Oh, C., and Sorensen, C.M. (1997). The Effect of Overlap between Monomers on the Determination of Fractal Cluster Morphology. J. Colloid Interface Sci. *193*, 17–25.
53. Wang, Z., Bi, L., Wang, H., Wang, Y., Han, W., and Zhang, X. (2022). Evaluation of a new internally-mixed aerosol optics scheme in the weather research and forecasting model. J. Quant. Spectrosc. Radiat. Transf. *283*, 108147. https://doi.org/10.1016/j.jqsrt.2022.108147.

STAR★METHODS

KEY RESOURCES TABLE

REAGENT or RESOURCE	SOURCE	IDENTIFIER
Chemicals, peptides, and recombinant proteins		
Standard reference materials for the analysis of mixed cation components in water via ion chromatographs	National Testing Center for Non ferrous Metals and Electronic Materials	GNM-M050377-2013
Standard reference materials for the analysis of mixed anionic components in water via ion chromatographs	National Sharing Platform for Reference Materials	GBW(E)130433
Carbon Support Membrane (Imported Copper Mesh)	Tianld Co., China	carbon Type-B, 300-mesh copper
PTFE Hydrophilic Membrane Filters, 0.22 mm, 33 mm	Jiangsu Green Union	RSF33TS1A
Critical commercial assays		
PM_{10} sampler	*Qingdao Jinshida Electronic Technology Co., Ltd., China*	KB-120F
Portable sampler	Genstar Electronic Technology, China	DKL-2
Microscope	OLYMPUS	BX51M
Transmission electron microscope	JEOL, Japan	JEM-2100
Energy-dispersive X-ray spectrometer	Oxford Instruments, United Kingdom	INCA X-Max^N 80T
Atomic force microscope	Bruker, Germany	DIMENSION icon with ScanAsyst, USA
Sunset Organic Carbon and Elemental Carbon Analyzer	Sunset Laboratory Inc.	Model 5L
Dionex™ ICS-600 Starter Line IC	Thermo Scientific	ICS-600
X-ray fluorescence spectrometer	Malvern Panalytical	Epsilon 4
Deposited data		
Data for Figures 2 and 4	This paper	https://doi.org/10.6084/m9.figshare.22086281
Software and algorithms		
Hybrid Single-Particle Lagrangian Integrated Trajectory model	NOAA Air Resources Laboratory	https://www.ready.noaa.gov/HYSPLIT.php
Python version 2.7	Python Software Foundation	https://www.python.org
Origin 2023b	OriginLab	https://www.originlab.com/
Radius	EMSIS GmbH	https://www.emsis.eu/products/radius
NanoScope Analysis software 2.0	Bruker, Germany	https://www.bruker.com/en/services/software-downloads.html

RESOURCE AVAILABILITY

Lead contact

Further information and requests for resources and reagents should be directed to and will be fulfilled by the lead contact, Weijun Li (liweijun@zju.edu.cn).

Materials availability

This study did not generate new unique materials.

Data and code availability

- Microscopy data reported in this paper will be shared by the lead contact upon request. Data for Figures 2 and 4 have been deposited at figshare and are publicly available as of the date of publication. DOIs are listed in the key resources table.
- This paper does not report original code.
- Any additional information required to reanalyze the data reported in this paper is available from the lead contact upon request.

METHOD DETAILS

Aerosol collection and measurement

Samples were collected at Lulang station in the South-East Tibetan Plateau Station for Integrated Observation and Research of Alpine Environment (29°45′58.77″ N, 94°44′17.68″ E, 3330 m a.s.l.) from 8 April to 21 April 2021 during the premonsoon season. The Lulang station is in the valley of the Yarlung Tsangpo Grand Canyon, a transport channel for the warm-humid Indian monsoon (Figure 1). The nearest village is 2 km south of the Lulang station. The Fire Information during the sampling period is provided by https://firms.modaps.eosdis.nasa.gov/map/.

A KB-120F sampler (Qingdao Jinshida Electronic Technology Co., Ltd., China) with a flow rate of 100 L min^{-1} was used to collect PM_{10} samples on 90 mm diameter quartz filters for 11.5 h (daytime is 08:00–19:30 Beijing time; nighttime is 20:00–07:30 Beijing time of the next day). The chemical composition, i.e., water-soluble inorganic ions (WSII), metals, organic carbon (OC), and elemental carbon (EC) were measured according to our recent studies.[36] The temperature program is NOISH870 for OC and EC. Concentrations of organic matter (OM) were calculated by multiplying OC concentrations by a factor of 1.8.[49,50] The total mass concentrations of water-soluble inorganic ions were recorded as TWSII, including Na^+, NH_4^+, K^+, Mg^{2+}, Ca^{2+}, F^-, Cl^-, SO_4^{2-}, and NO_3^-.

Individual particle collection and morphological analysis

Individual aerosol particles were collected by a portable sampler (DKL-2, Genstar Electronic Technology, China) with two jet nozzles at 0.3 mm and 0.5 mm as the sampler inlet. The sample filters were copper grids coated with carbon film (carbon Type-B, 300-mesh copper; Tianld Co., China) and silicon wafers. Individual particle samples were collected at the following Beijing times: 3:00, 9:00, 15:00, and 21:00 for 20 to 40 min and stored in plastic capsules under low relative humidity (RH = 20-25%). We preliminarily used a microscope (OLYMPUS, BX51M) to check the particle distribution in the sample filters,[36] and then 21 aerosol samples were suitable for TEM analyses and selected. Finally, we analyzed 4947 particles by TEM (JEOL JEM-2100, Japan) combined with an energy-dispersive X-ray spectrometer (EDS, INCA X-Max^N 80T, Oxford Instruments, United Kingdom). RADIUS software (EMSIS GmbH, Germany) was applied to measure the morphological parameters of individual particles in TEM images.

Roundness (RN) is defined as the ratio of the projected area of the particle to the area of a circle with its diameter equal to the longest dimension (Equation 4).

$$RN = \frac{4A_a}{\pi L_{max}^2} \quad \text{(Equation 4)}$$

where RN is the roundness of an individual particle. A_a is the projected area and L_{max} is the longest dimension via RADIUS.

According to China et al.[25] and Wang et al.,[22] we used the fractal dimension (D_f) to further identify the differences in three types of soot-bearing particles. D_f is characterized using the scaling law in Equation 5.

$$N = k_g\left(\frac{2R_g}{d_p}\right)^{D_f} \quad \text{(Equation 5)}$$

where k_g is the fractal prefactor. D_f is the fractal dimension. The diameter of the monomer is d_p. R_g is the radius of gyration of the soot and can be obtained by the simple correlation in Equation 6.[22] N is the total number of monomers in each soot, which can be calculated in Equation 7.[51]

$$L_{max} / (2R_g) = 1.50 \pm 0.05 \quad \text{(Equation 6)}$$

$$N = k_a\left(\frac{A_a}{A_p}\right)^a \quad \text{(Equation 7)}$$

where L_{max} is the maximum length of the soot. A_a is the projected area of the soot particle. A_p is the mean projected area of the soot monomer. The values of a and k_a depend on the overlap parameter (δ) by referring to Oh and Sorensen[52] (their Figure 6).

The δ is defined using Equation 8.

$$\delta = \frac{2r}{l} \quad \text{(Equation 8)}$$

where δ is the overlap parameter. r is the soot monomer radius and l is the monomer spacing. In this study, we used the TEM images to obtain that: the average d_p is 33.4 nm; a is 1.08, 1.16, 1.18 for bare-like soot, partly-coated soot and embedded soot, respectively; k_a is 1.50, 1.80, 2.05 for bare-like soot, partly-coated soot, and embedded soot, respectively.

The individual particles on the silicon wafers were measured using atomic force microscope (AFM, DIMENSION icon with ScanAsyst, Bruker, Germany) with a digital nanoscope IIIa in tapping mode. A 10 μm × 10 μm scanning range and 0.5-0.8 Hz scanning rate were selected. A total of 286 particles were analysed by the NanoScope Analysis software (2.0, Bruker, Germany) to obtain the bearing area (A) and bearing volume (V) of each particle. The equivalent circle diameter (ECD) and equivalent volume diameter (EVD) of individual particles could be calculated as Equations 9 and 10.

$$ECD = \sqrt{4A/\pi} \quad \text{(Equation 9)}$$

$$EVD = \sqrt[3]{6V/\pi} \quad \text{(Equation 10)}$$

Linear regression between ECD and EVD yielded "EVD = 0.562 × ECD" with an R^2 of 0.973, and $p < 0.01$ (Figure S12). Therefore, a factor of 0.562 was adopted to transform the ECD to EVD for all particles in the TEM images.

Mixing rules for soot-bearing particles in the models

We noticed that soot-bearing particles might have multi-soot cores.[23,38] We summed multi-soot cores as Equation 11.

$$EVD_c = \sqrt[3]{\sum_i^{n_{soot}} (EVD_{core,i})^3} \quad \text{(Equation 11)}$$

where EVD_c is the cumulative equivalent volume diameter of all soot cores in an individual particle, nm. n_{soot} is the number of soot cores. The EVD of the ith soot core is $EVD_{core,\ i}$, nm. D_p/D_c is calculated as the ratio between the EVD of an individual particle and EVD_c.

Equation 11 shows a sophisticated mixing structure with multi-soot cores in a particle. It is completely different from the well-known core-shell structure, in which soot is a spherical core surrounded by a uniform coating.[44,53] Chylek et al.[47] and Jacobson[40] developed a method by using the dynamic effective medium approximation (DEMA) to calculate optical characteristics for particles with multi-soot cores. We transform Equation 1 of the Jacobson[40] into a form containing n_{soot} in Text S4. DEMA assumed that the same cores were distributed randomly in an individual particle.[8,13] In other words, the mixing rule of DEMA simplifies Equation 11 to Equation 12.

$$EVD_c = \sqrt[3]{n_{soot}} \times EVD_{core,DEMA} \quad \text{(Equation 12)}$$

Model studies set $EVD_{core,DEMA}$ as 100 or 200 nm.[8,40] As a result, the heterogeneity of D_p/D_c is determined by the n_{soot} involved in a selected size bin (e.g., $D_p = 1000 \pm 100$ nm), rather than the heterogeneity of the coating thickness from condensing on the surface of different soot core. Meanwhile, n_{soot} can be a decimal in the model, e.g., 0.25 in Jacobson,[40] which is a counterfactual assumption. Therefore, n_{soot} is an important input for DEMA, but observational evidence was rare to understand how a bare-like soot aged into a particle with multi-soot cores.[48] Table S7 shows a case for $D_p = 1000 \pm 100$ nm, that we constructed a theoretical relationship between D_p/D_c and D_c by setting $EVD_{core,DEMA}$ as 100 or 200 nm and using the true distribution of n_{soot} from TEM images.